J Mater Sci (2020) 55:7530–7545

Metals & corrosion

Strengthening mechanisms of creep-resistant 12%Cr–3%Co steel with low N and high B contents

I. Nikitin[1], A. Fedoseeva[1,*], and R. Kaibyshev[1]

[1] *Belgorod National Research University, Pobeda 85, Belgorod, Russia 308015*

Received: 16 December 2019
Accepted: 22 February 2020
Published online: 9 March 2020

ABSTRACT

The contributions from the martensitic laths, dislocations, secondary phase particles, and supersaturated solid solutions to the overall strength of the 12%Cr–3%Co–2.5%W creep-resistant steel with low N and high B contents were calculated after various heat treatments consisting of normalizing followed by medium-temperature tempering. An increase in the normalizing temperature from 1050 to 1150 °C led to an increase in the average size of the prior austenitic grains from 44 to 68 μm, but the δ-ferrite fraction did not significantly change. Medium-temperature tempering in the range of 750–800 °C ensured the formation of a tempered martensite lath structure with an average martensitic lath/subgrain size of 0.23–0.34 μm, along with a high dislocation density inside the laths/subgrains, fine secondary phase particles such as $M_{23}C_6$ carbides along the boundaries of the prior austenite grains, packets, blocks, and martensitic laths/subgrains, and (Ta,Nb)X carbonitrides uniformly distributed inside the matrix. After medium-temperature tempering in the range of 750–800 °C, the ferritic matrix was supersaturated with substitutional elements such as Cr, W, Mo, and Cu. An increase in the tempering temperature from 750 to 800 °C led to decreases in the yield strength and ultimate tensile strength by 16.2% and 10.5%, respectively, as well as an increase in the elongation of 43.8%. The main contributions to the overall strengthening of the steel investigated after the different heat treatment regimens produced solid solution strengthening and precipitation hardening, which were independent of the tempering temperature, as well as lath boundary and dislocation strengthening, which was strongly dependent on the tempering temperature. Different approaches for evaluating the strengthening mechanisms and their contributions to the yield strength were applied, and the results are discussed.

Address correspondence to E-mail: fedoseeva@bsu.edu.ru

https://doi.org/10.1007/s10853-020-04508-7

Introduction

The modern development of power engineering has the goal of increasing the amount of combustible solid fuel for coal-fired power plants and decreasing harmful emissions (including carbon dioxide) to the atmosphere by increasing the combustion temperature [1–3]. This can be achieved by commissioning power units operating at ultra-supercritical (USC) steam parameters, namely a steam pressure of 25–30 MPa and temperature of 600–620 °C, which are unattainable for traditional ferritic steels [1–3]. The transition to USC steam parameters has increased the efficiency of power units from 36 to 40–44% compared to the power units developed in the early 1960s [2]. High-Cr martensitic steels with low nitrogen and high boron contents, which retain their creep resistance and corrosive properties under extreme conditions, are prospective materials for manufacturing the elements of new coal-fired power units operating at USC steam parameters. In addition to a high creep resistance, these steels also have a relatively low cost, which ensures that their use is very efficient [1–10]. The strengthening of these steels is achieved by the formation of a tempered martensite lath structure (TMLS), which has a strict hierarchical structure and high dislocation density inside the martensitic laths, after medium-temperature tempering. The boundaries of the TMLS are stabilized by nano-sized $M_{23}C_6$ carbides, which provide a high drag Zener pressure and restrain the migration of the lath/subgrain boundaries [1, 4, 10–13]. Non-equilibrium nano-sized MX carbonitrides (where M represents V, Nb, Ti, and/or Ta, and X represents C and/or N) precipitate inside the martensitic laths and serve as obstacles to the rearrangement of the mobile dislocations into more stable configurations or embedding in the already existing irregular dislocation boundaries [6, 8, 11, 14]. Moreover, after medium-temperature tempering, the solid solution is supersaturated with substitutional elements such as chromium, tungsten, molybdenum, and copper.

The various strengthening mechanisms for high-Cr martensitic steels could contribute to the yield strength, including structural strengthening by the basic Hall–Petch model [15–17], substructural strengthening by the Langford–Cohen model [18–30], dislocation strengthening by the Taylor equation [31], precipitation hardening by the Orowan mechanism [32], and solid solution strengthening due to the interstitial and substitutional elements [33, 34]. At the same time, the contributions of these factors can be considered in combinations that are more complex than simple addition [23, 35–37]. For martensitic and bainitic steels with a lamellar structure, numerous studies have focused on modeling and predicting the relationship between the microstructure and mechanical properties [19–30]. Now, special attention is given to the structural strengthening, which is often overestimated [27–29]. Moreover, the data found in the literature do not agree on the mechanisms that should be taken into account and in which combinations. The aim of the present research was to consider different approaches to estimating the strengthening contributions from various mechanisms and analyzing the contributions of different mechanisms to the yield strength of 12%Cr–3%Co steel with low N and high B contents.

Materials and methods

Co-modified 12%Cr steel with a chemical composition (in wt%) of Fe_{bal}–0.11C–0.02Si–0.03Ni–0.04Mn–11.4Cr–3.0Co–0.6Mo–2.5W–0.76Cu-0.2V–0.04Nb-0.07Ta–0.01B–0.003N was prepared using vacuum-induction melting at the Department of Ferrous Metallurgy (IEHK), Aachen, Germany. This provided the low N, Mn, Ni, S, P, and Al contents and high B content. Square 110 mm × 110 mm billets with a thickness of 40 mm were cut off, homogenized at a temperature of 1150 °C for 16 h, and subjected to hot-forging at a temperature of 1150 °C. The heat treatment of the 12%Cr–3%Co steel consisted of normalizing at temperatures of (1050 ± 10) °C, (1070 ± 10) °C, (1100 ± 10) °C, and (1150 ± 10) °C for 1 h; air cooling; subsequent tempering for 3 h at temperatures of (750 ± 10) °C, (770 ± 10) °C, and (800 ± 10) °C; and air cooling. Tensile tests were performed on flat samples with a length of 35 mm and cross section of 7 mm × 3 mm using a strain rate of 2×10^{-3} s^{-1} at room temperature.

Microstructural characterization was performed using an Olympus GX70 optical microscope (OM), a JEM-2100 transmission electron microscope (TEM) operated at 200 kV and equipped with an INCA energy-dispersive X-ray spectrometer (EDS), and a Quanta 600 scanning electron microscope (SEM). To reveal the size of the prior austenite grains, the OM samples were ground, polished, and etched in a

solution of 2% HNO_3 and 1% HF in water. The fraction of δ-ferrite was estimated by a linear intercept method using OM images. For the TEM examinations, disks with a diameter of 3 mm were electropolished to perforation with a Tenupol-5 twinjet polishing unit using a 10% solution of perchloric acid in glacial acetic acid. In addition, carbon extraction replicas on nickel grids were used to analyze the morphology, chemical composition, and nature of the dispersoids. The replicas were prepared by mechanical polishing using emery paper and a 3-μm silica suspension, followed by electrochemical etching in a solution of 10% hydrochloric acid in ethanol at 2 V for 1 min. The transverse lath size was measured on at least six arbitrarily selected typical TEM images for each data point using a linear intercept method, counting all of the clearly defined boundaries. The dislocation observation was carried out under multiple-beam conditions with large excitation vectors for several diffracted planes for each TEM image. The other details of the structural characterization were reported in previous works [6, 15, 21–23, 36–40]. Modeling of the phase composition was carried out using Thermo-Calc software (TCFE7 database) for a chemical composition (in wt%) of Fe_{bal}–0.1C–11.4Cr–0.6Mo–2.5W–3.0Co–0.2V–0.04Nb–0.07Ta–0.003N–0.01B. Only the experimentally observed phases were chosen for modeling.

Experimental results

Microstructure after normalizing

The normalizing of the 12%Cr–3%Co steel was carried out at four temperatures: 1050 °C, 1070 °C, 1100 °C, and 1150 °C for 1 h, followed by air cooling. The selection of normalizing temperatures was based on the ratio between the fraction of (Ta,Nb)X carbonitrides and the prior austenite grain (PAG) size. The less amount of (Ta,Nb)X carbonitrides is, the more PAG size is (Fig. 1). The PAG size affects the creep properties and impact toughness [1]. The minimum creep rate is inversely proportional to the PAG size when the PAG size is smaller than 50 μm [1]. So, the PAG size should be controlled to be about 50 μm to obtain the highest creep resistance. Increasing the normalizing temperature led to the dissolution of (Ta,Nb)X particles and an increase in the PAG size from 44 ± 2 μm at 1050 °C to

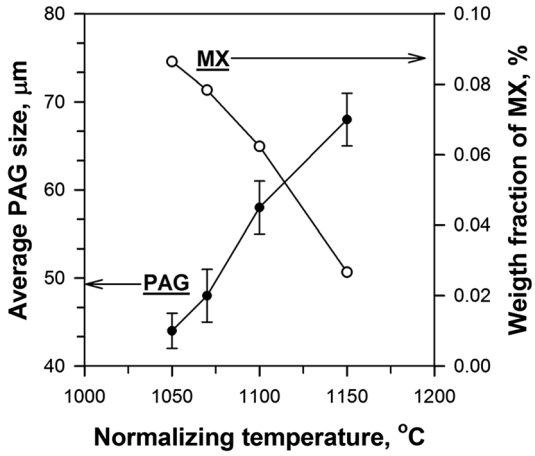

Figure 1 Temperature dependence of average PAG size and fraction of MX carbonitrides.

68 ± 5 μm at 1150 °C (Figs. 1, 2). Simultaneously, δ-ferrite was observed at all of the normalizing temperatures. An increase in the normalizing temperature did not lead to a significant increase in the δ-ferrite fraction; the fraction of δ-ferrite was approximately 10% at all of the normalizing temperatures (Fig. 2). The normalizing temperature of 1070 °C provided an average PAG size of 48 ± 3 μm and an acceptable amount of δ-ferrite.

Microstructure after tempering

The tempering of the 12%Cr–3%Co steel was performed at temperatures of 750 °C, 770 °C, and 800 °C. The selection of the tempering temperatures was based on the standard regimens for the heat treatment of 9–12%Cr martensitic steels [1–3]. The standard tempering temperature for high-Cr martensitic steels lies in the range of 720–800 °C, which provides the maximum creep resistance, yield strength, and joinability because of the TMLS formation. The lowest tempering temperature for the high-Cr martensitic steels was related to the temperature for starting the precipitation of VN nitrides with a size greater than 8 nm; the highest temperature was limited by the temperature for starting the subgrain structure formation because of the recovery and polygonization of the quenched martensite structure [1, 2, 41, 42]. Because the nitrogen content of the 12%Cr–3%Co studied steel decreased to 0.003%, the precipitation of VN nitrides after tempering in the temperature range of 700–800 °C was not revealed. Moreover, tempering temperatures lower than

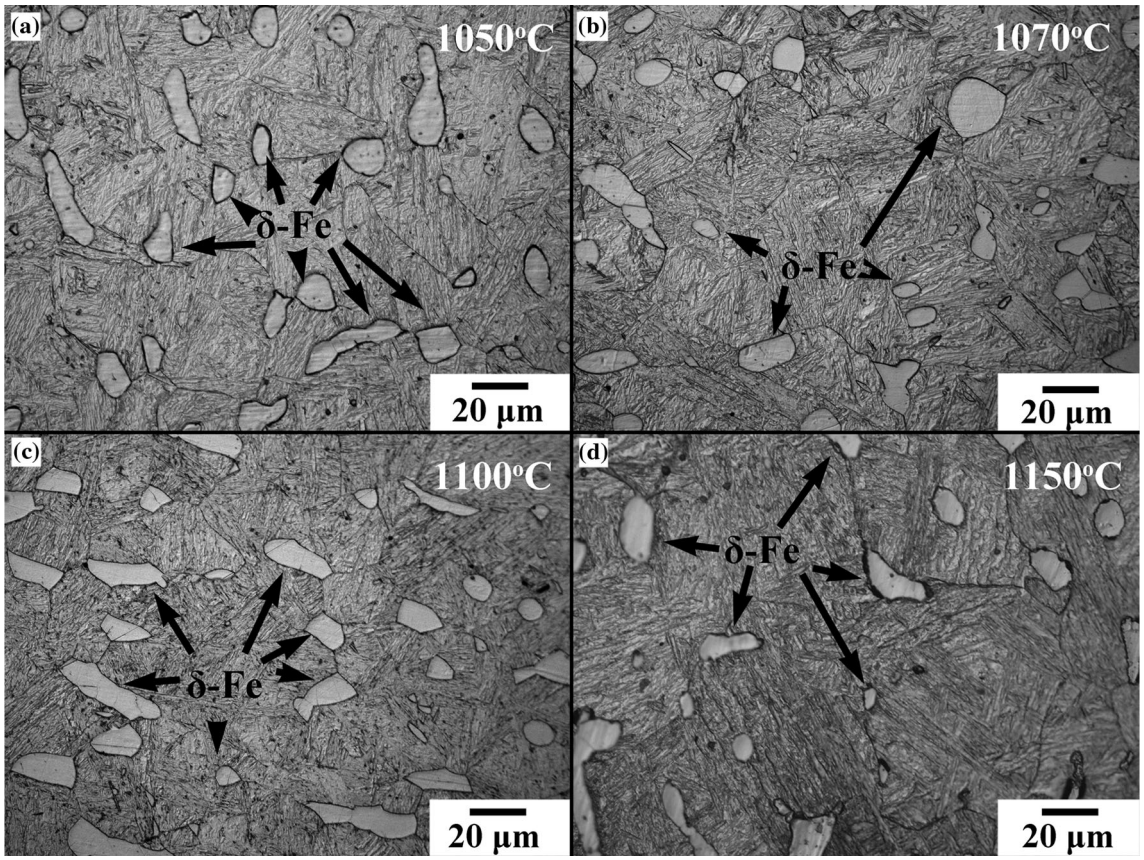

Figure 2 OM images of quenched structures of 12%Cr–3%Co martensitic steel after normalizing at 1050 °C (**a**), 1070 °C (**b**), 1100 °C (**c**) and 1150 °C (**d**).

750 °C did not provide the high fraction of $M_{23}C_6$ carbides along the boundaries of the martensitic laths or subgrains. SEM and TEM images of the structure of the 12%Cr–3%Co steel after tempering at T = 750 °C, 770 °C, and 800 °C are presented in Figs. 3 and 4, respectively. After tempering at T = 750 °C and 770 °C, the TMLS was dominant, and only a few subgrains were revealed. The average transverse sizes of the martensitic laths were 0.23 and 0.29 μm after tempering at T = 750 °C and 770 °C, respectively (Table 1). In contrast, after tempering at T = 800 °C, both the TMLS and subgrain structure with an average subgrain size of 0.34 μm were observed (Table 1). The high dislocation density inside the martensitic laths/subgrains slightly decreased when the tempering temperature increased (Table 1). Regardless of the tempering temperature, $M_{23}C_6$ carbides with an average size of approximately 50 nm (Figs. 3, 4, Table 1) contained ~ 70 wt% Cr, ~ 25 wt% Fe, and ~ 5 wt% Mo, and were located along the boundaries of the PAGs, packets, blocks, and martensitic laths/subgrains. $M_{23}C_6$ carbide was the dominant secondary phase (Fig. 4), with a volume fraction of approximately 2.23–2.26%, as obtained by the Thermo-Calc software, and it decreased with an increase in the tempering temperature (Table 1). Simultaneously, the size distribution of the $M_{23}C_6$ particles (Fig. 4d–e) did not depend on the tempering temperature. Regardless of the tempering temperature, both fine $M_{23}C_6$ particles with a mean size of 25 nm, which were mainly located along the boundaries of the low-angle martensite laths (the fraction of such particles was approximately 17%), and large $M_{23}C_6$ particles with sizes greater than 150 nm located along the PAG boundaries (the fraction of such particles did not exceed 5%) were revealed in the tempered structure of the steel studied. Despite the fact that the average size of the $M_{23}C_6$ particles was very small, approximately 50 nm, which was almost half the size of those in the 9%Cr–3%Co steels [11–13, 38, 42], a wide size distribution indicated a rapid coarsening tendency

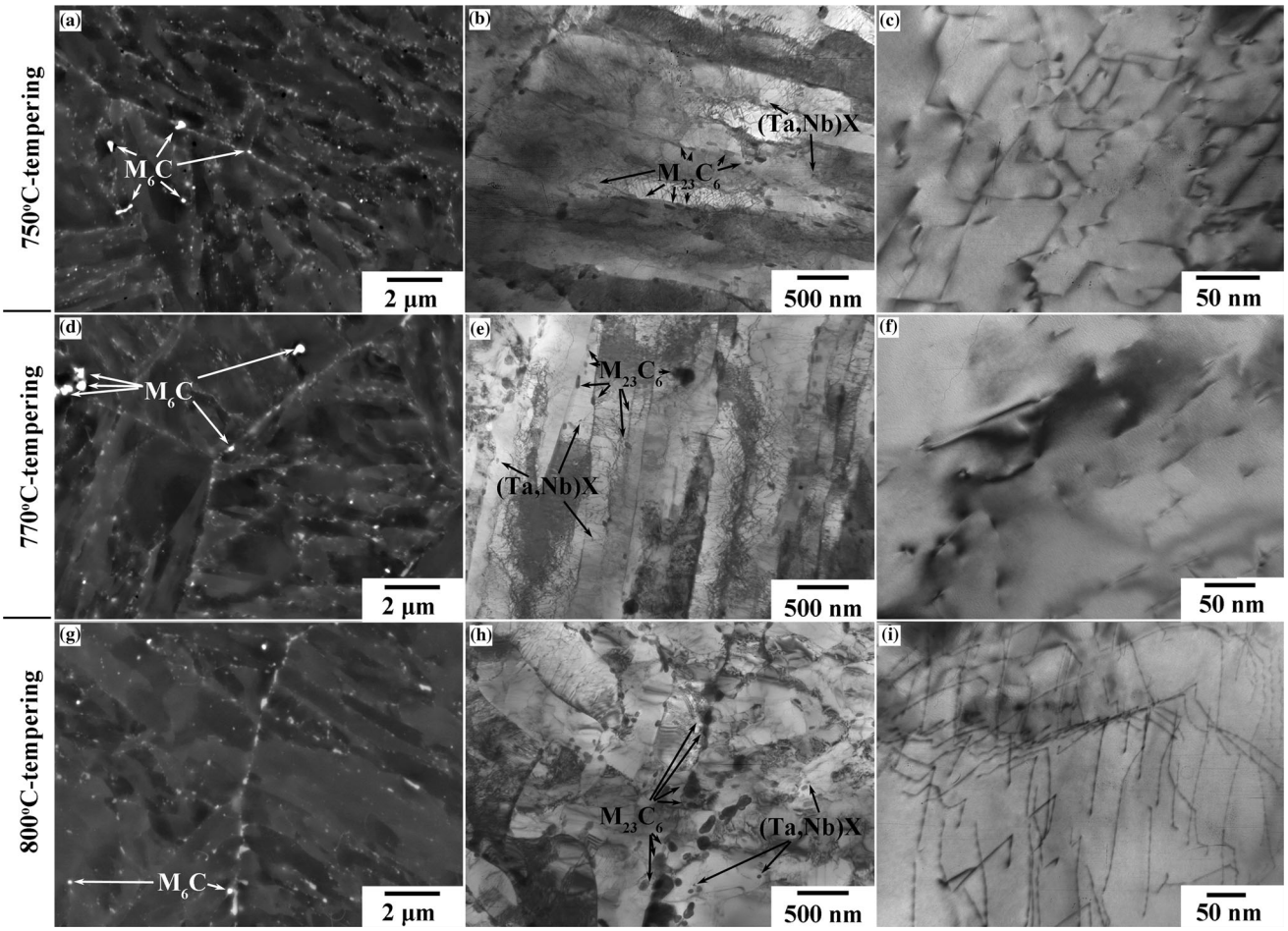

Figure 3 SEM (**a**, **d**, **g**) and TEM (**b**, **c**, **e**, **f**, **h**, **i**) images of tempered structures of 12%Cr–3%Co martensitic steel after various heat treatment regimes.

for these particles upon creep testing because of the creation of a driving force.

In addition, several M_6C (Fe_3W_3C) particles with average sizes of 117, 155, and 165 nm were detected along the boundaries of the PAGs and blocks after tempering at $T = 750$ °C, 770 °C, and 800 °C, respectively (Figs. 3a, d, g, 4b). M_6C particles were also detected along the boundaries between the martensite and δ-ferrite. These particles contained up to 40 wt% W. Moreover, no Laves phase particles were detected during tempering under any conditions. In previous investigations [11, 43], the precipitation of M_6C carbides also occurred in some steels with a high Cr and/or W content as an intermediate metastable phase before the precipitation of the Laves phase. Their volume fraction was negligible, and they did not play a significant role in the hardening of the steel. For this reason, they will not be considered in the following discussion.

(Ta,Nb)-rich MX carbonitrides were homogeneously distributed within martensitic matrix (Fig. 4). These had a round shape and contained ~ 77–87 wt% Ta, ~ 5–7 wt% Nb, and ~ 7–13 wt% Cr + Fe. The mean size of these particles increased with the tempering temperature from 40 nm at $T = 750$ °C to 60 nm at $T = 800$ °C. A volume fraction of 0.08% was estimated by the Thermo-Calc software and was independent of the tempering temperature (Table 1). The precipitation of secondary phase particles enriched by Cr, Fe, Mo, Ta, Nb, C, and N decreased the content of these elements in the solid solution. Thus, after tempering in the temperature range of 750–800 °C, the supersaturated solid solution included 10.5 wt% Cr, 3.0 wt% Co, 2.1 wt% W, 0.5 wt% Mo, 0.2 wt% V, and 0.78 wt% Cu.

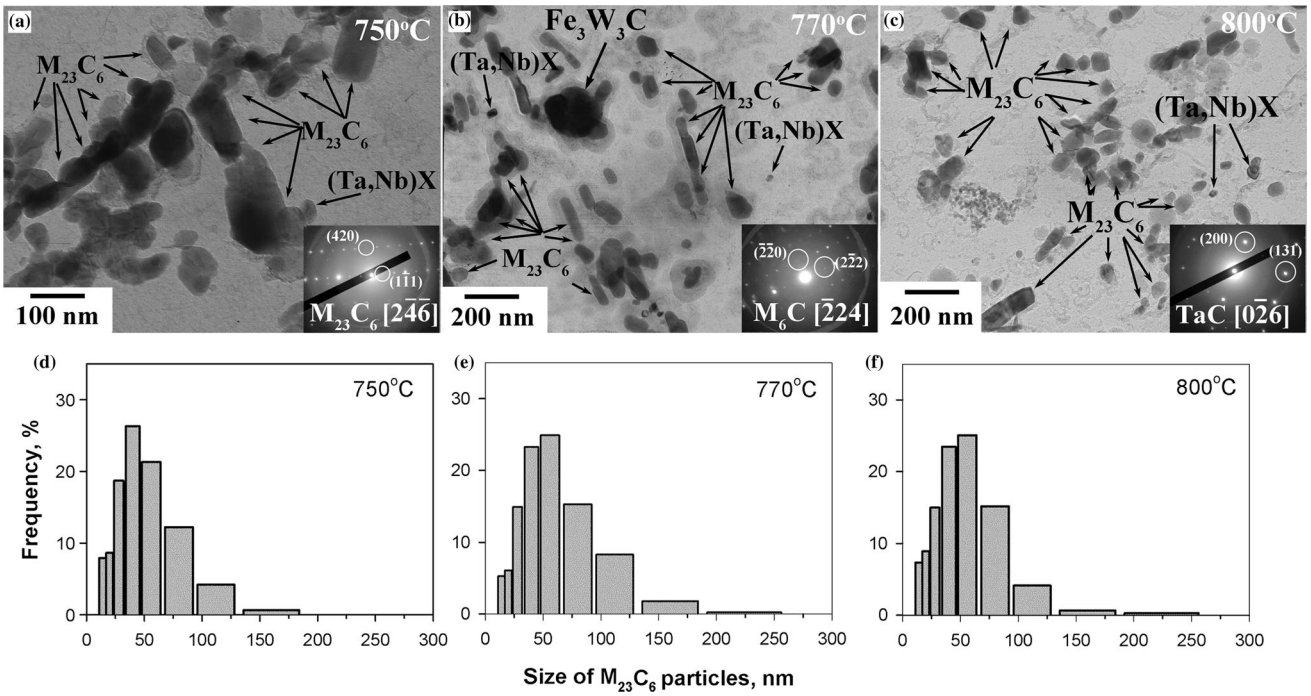

Figure 4 TEM images of secondary phase particles on carbon replicas **a**–**c** in tempered structure of 12%Cr–3%Co martensitic steel after tempering at T = 750 °C (**a**), 770 °C (**b**), and 800 °C (**c**); along with size distributions of $M_{23}C_6$ carbides after tempering at T = 750 °C (**d**), 770 °C (**e**), and 800 °C (**f**).

Table 1 Structural parameters after various heat treatment regimens

Structural parameters	750 °C tempering	770 °C tempering	800 °C tempering
Mean PAG size, μm	48 ± 5	48 ± 5	48 ± 5
Mean block size, μm	1.9 ± 0.2	1.9 ± 0.2	1.9 ± 0.2
Mean size of martensitic laths μm	0.23 ± 0.05	0.29 ± 0.05	0.34 ± 0.05
Mean subgrain size, μm	–	–	0.35 ± 0.05
Dislocation density, × 10^{14} m^{-2}	3.2 ± 0.1	2.0 ± 0.1	1.9 ± 0.1
Mean size of $M_{23}C_6$ carbides, nm	46 ± 5	55 ± 5	50 ± 5
Volume fraction of $M_{23}C_6$ (Thermo-Calc), %	2.26	2.25	2.23
Mean size of (Ta,Nb)X carbonitrides, nm	40 ± 5	50 ± 5	60 ± 5
Volume fraction of (Ta,Nb)X (Thermo-Calc), %	0.08	0.08	0.08
Content of Cr in matrix, wt%	10.4 ± 0.1	10.4 ± 0.1	10.5 ± 0.1
Content of W in matrix, wt%	2.04 ± 0.1	2.17 ± 0.1	2.17 ± 0.1
Content of Mo in matrix, wt%	0.48 ± 0.1	0.51 ± 0.1	0.54 ± 0.1
Content of Co in matrix, wt%	2.90 ± 0.1	2.92 ± 0.1	2.95 ± 0.1

Mechanical properties

When the tempering temperature decreased, the strength properties of the 12%Cr–3%Co steel increased and the plasticity decreased (Fig. 5). Thus, a decrease in the tempering temperature from 800 to 750 °C gave increases of 111 MPa in the yield strength and 87 MPa in the ultimate tensile strength. Therefore, the elongation decreased from 23 to 16% when the tempering temperature decreased from 800 to 750 °C. Additionally, the elastic limit was estimated to calculate the work hardening of the steel studied during the tensile tests. Increasing the tempering temperature did not affect the elastic limit, which was ~ 46–49 MPa.

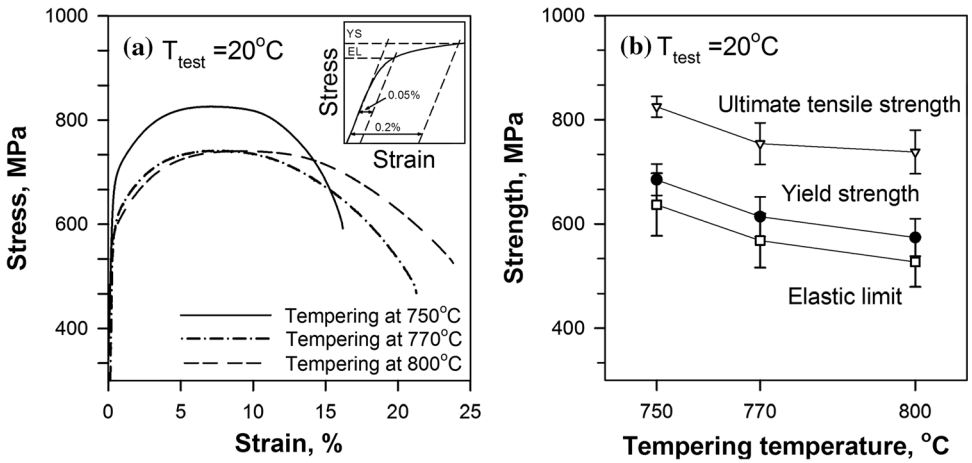

Figure 5 Engineering tensile curves for 12%Cr–3%Co martensitic steel after various heat treatment regimens (**a**), and temperature dependences of ultimate tensile strength, yield strength, and elastic limit (**b**), where tensile tests were carried out at room temperature. YS and EL in (**a**) mean yield strength and elastic limit, respectively.

Discussion

Types of strengthening

Strengthening due to lattice friction (Peierls stress σ_i)

Peierls stress is the stress that is required to move a dislocation through an ideal lattice. The simplest estimation of this stress is $2 \times 10^{-4} \times G$, where G is the shear modulus, which is 8.4 GPa at 20 °C [19, 44, 45]. Experimental estimations of the lattice friction in α-iron at room temperature lie in the range of 13–55 MPa. In one study [23], a value of 41 MPa was used for steel with 0.4% C; in another study [26], a value of 30 MPa was used for steel with 0.1% C. In the present study, a value of 17 MPa was used for 12% Cr–3% Co steel containing 0.1% C.

Solid solution strengthening due to substitutional alloying elements (σ_{ss})

In this work, it was assumed that after tempering, the interstitial elements (C, N, B) were not dissolved in the solid solution, but were in a bound state in the composition of the secondary phase particles. Solid solution strengthening was provided by substitutional elements such as Cr, W, Mo, and Co. The effect of substitutional elements such as Si, Ni, Mn, and Al was not taken into account because of the negligible contents of these elements in the matrix. The influence of Cu and V was also not taken into account. The contribution from solid solution hardening can be estimated as follows (1):

$$\sigma_{ss} = \sum_{i=1}^{n} K_i C_i^n, \quad (1)$$

where K_i is the coefficient of solid solution strengthening when the alloying element is dissolved in ferrite (MPa/%n), and Ci is the concentration of the alloying element dissolved in ferrite (wt% or at%). Experimental data on the coefficients (Ki) of solid solution strengthening in a ferritic matrix were systematized in [33]. The present study used the coefficients (K_i) that were previously reported in [26, 33, 46]. The exponent $n = 3/4$ is applicable for the Cr, W, and Mo substitutional elements in ferrite when calculating the solid solution strengthening [31, 32, 47]. To calculate the strengthening from Co, the yield strength of Co-modified P911 steel was compared with that of Co-free P911 steel [46]. The results of the calculations are given in Table 2.

Dislocation strengthening (σ_{disl})

The contributions from dislocations to the overall strength could be estimated using an equation that was originally proposed by Taylor (2) [23, 26, 31]:

$$\sigma_{\text{disl}} = \alpha G b \sqrt{\rho} \quad (2)$$

where α is an iron polycrystalline constant (0.38) [23, 24, 26], G is the shear modulus (8.4 GPa at 20 °C)

Table 2 Solid solution strengthening due to substitutional elements in α-iron

Elements	K_i (MPa/%^{n})	$\Delta\sigma_{ss}$, MPa	References
W	75.79	53.6–56.1	[26, 33]
Mo	66.14	25.7–27.5	[26, 33]
Cr	9.65	59.5–59.9	[26, 33]
Co	21.88	63.5–65.0	[46]

[19, 44, 45], b is the Burger vector (2.48×10^{-10} m, assuming all of the dislocations in the steel have a Burger vector of the type $\frac{1}{2}(111)$), and ρ is the total dislocation density (m^{-2}). The average dislocation densities were 3.2×10^{14}, 2.0×10^{14}, and 1.9×10^{14} m^{-2} after tempering at T = 750 °C, 770 °C, and 800 °C, respectively (Table 1). The contributions from dislocations calculated by formula (2) were 142, 112, and 109 MPa after tempering at T = 750 °C, 770 °C, and 800 °C, respectively.

In one study [30], the following linear relationship between the transverse size of martensitic laths and the dislocation density was proposed (3):

$$l = \frac{A}{\sqrt{\rho}} + B \tag{3}$$

where A and B are the slope and intercept of the linear regression, respectively (Fig. 6); l is the mean transverse size of the martensitic laths/subgrains (μm), and $1/\sqrt{\rho}$ is the distance between dislocations (μm). The linear regression between the mean transverse size of the martensitic laths/subgrains and the dislocation density for the 12%Cr–3%Co steel is represented in Fig. 6.

Expression (3) could be rewritten as (4) [30]:

$$\rho^{0.5} = A/(l - B) \tag{4}$$

Using the linear relationship between the mean transverse size of the martensitic laths/subgrains and the dislocation density, the strengthening due to laths/subgrains with low-angle boundaries can be expressed by the dislocation strengthening, by substituting expression (4) into Eq. (2), as suggested in [30]:

$$\sigma_{\text{disl 1}} = \alpha G b A/(l - B) \tag{5}$$

The contributions from dislocations calculated using formula (5) were 141, 120, and 104 MPa after tempering at T = 750 °C, 770 °C, and 800 °C, respectively. Note that the values of the contributions from dislocations estimated by Eqs. (2) and (5) were similar.

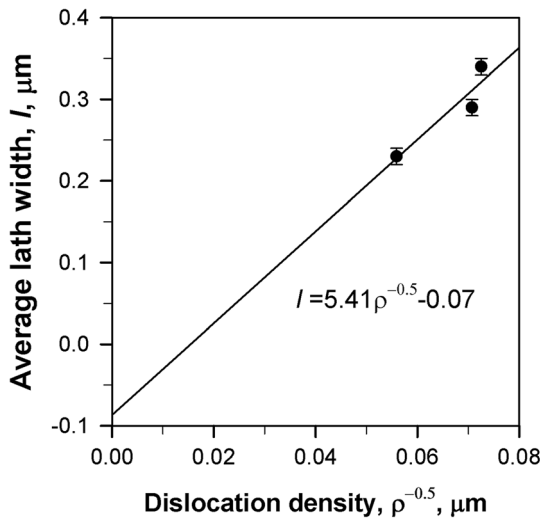

Figure 6 Linear dependences of transverse width of martensitic laths/subgrains on reciprocal square dislocation density for 12%Cr–3%Co martensitic steel after various heat treatment regimes.

Work hardening upon tensile testing (σ_{wh})

During tensile tests at ambient temperature, the formation of additional dislocations occurred, which were not taken into account when calculating the dislocation strengthening. This contribution was estimated as the difference between the yield strength and the elastic limit. For steels with a carbon content of 0.4 wt% C, this value was 65 MPa [23]. For steels with a carbon content of 0.1 wt%, the authors of [26] assumed that the value of work hardening would be approximately 40 MPa, but this assumption was made theoretically, not based on experimental data. For the studied steel with a C content of 0.1 wt%, the differences between the yield strength and elastic limit were 49, 46, and 47 MPa after tempering at T = 750 °C, 770 °C, and 800 °C, respectively (Fig. 4).

Precipitation strengthening due to $M_{23}C_6$ carbides and (Ta,Nb)X carbonitrides (σ_{part})

In the present work, it was assumed that the hardening from $M_{23}C_6$ carbides and (Ta,Nb)X carbonitrides could be estimated using an equation proposed by Orowan and modified by Humphreys (6) [32], which assumes that all of the particles are homogeneously distributed within a matrix:

$$\sigma_{\text{part}} = \frac{0.84Gb}{\lambda - d}, \tag{6}$$

where G is the shear modulus (GPa), b is the Burger vector (m), λ is the distance between particles (m), and d is the particle diameter (m). The distance between particles was estimated according to the following [32] (7):

$$\lambda = d\sqrt{\frac{\pi}{6f}} \tag{7}$$

where f is the volume fraction of particles. The average sizes of the secondary phase particles and their volume fractions estimated using the Thermo-Calc software are summarized in Table 1. Substituting the values from Table 1 into formulas (6) and (7) provides the contributions from the $M_{23}C_6$ carbides, which were 99, 83, and 91 MPa after tempering at T = 750 °C, 770 °C, and 800 °C, respectively, as well as the contributions from the (Ta,Nb)X carbonitrides, which were 18, 14, and 12 MPa after tempering at T = 750 °C, 770 °C, and 800 °C, respectively.

Strengthening due to grains with high-angle boundaries (σ_{HP})

The TMLS was a strictly hierarchical structure, in which the PAGs were divided into packets, and the packets were divided into blocks, which consisted of martensitic laths/subgrains. Only the martensitic lath/subgrain boundaries were low-angle ones and had a misorientation of less than 15°. The boundaries of the blocks, packets, and PAGs were high-angle ones with a misorientation of more than 15°. Thus, the minimum distance between high-angle boundaries corresponded to the block size. It is known that the relationship between the PAG and block dimensions can be described by the following empirical expression (8) [48]:

$$D_{\text{block}} = 0.04 D_{\text{PAG}} \tag{8}$$

where D_{block} is the mean block size, and D_{PAG} is the mean PAG size. Table 1 demonstrates that the average PAG and block sizes were independent of the tempering temperature; the average block size was 1.9 μm under all of the tempering conditions. The strengthening due to the grains with high-angle boundaries was calculated using the equation originally proposed by Hall–Petch (9) [15–17]:

$$\sigma_{H-P} = k_y d^{-1/2} \tag{9}$$

where d is the block size (μm), and k_y is a constant (MPa μm^{-2}). For the lamellar structure of bainite in the steel with a carbon content of 0.4 wt%, a value of 284.6 MPa μm^{-2} was used for the strengthening coefficient k_y [23]. Substituting the block size into Eq. (9), the contribution due to grain strengthening was found to be 206 MPa, regardless of the tempering temperature. The effect of δ-ferrite was not taken into account. In one study [49], the prediction of the reduction in yield strength due to the presence of δ-ferrite in TMLS was important for 12–15% Cr alloys, in which the δ-ferrite content can reach up to 60%. In the 12Cr–3Co steel studied, the δ-ferrite content was approximately 10%; according to [49], the yield strength values predicted with and without including the effect of 8% δ-ferrite were similar.

Strengthening due to laths/subgrains with low-angle boundaries (σ_{lath})

Many studies have used the transverse size of martensitic laths or the diameter of subgrains [18–30] as the size of grains in the Langford–Cohen model [18–20, 23, 26], in which the yield strength of iron was related to the reciprocal width of the cells rather than the reciprocal square root of this width, as required by the equation originally proposed by Hall–Petch. This gives the best fit with the experimental values (10):

$$\sigma_{\text{lath}} = k_{1y}(2l)^{-1} \tag{10}$$

where l is the mean transverse size of the martensitic laths/subgrains (μm), and k_{1y} is a constant (MPa μm^{-2}). In Eq. (10), ($2l$) is assumed to be double the mean transverse size of the martensitic laths/subgrains, as recommended in [50].

Many studies have been performed using different coefficients for the Langford–Cohen equation [18–28]. In the works [18, 20, 23, 26], the coefficient k_{1y} was 86.2 MPa μm^{-2}, which was the original value in the Langford–Cohen equation [18]. In the works [21, 22, 24, 25], the authors proposed a coefficient k_{1y} = 115–123 MPa μm^{-2}, noting that $k_{1y}(2l)^{-1}$ also took into account the dislocation density inside the grains [22]. In the works [27–29], the authors used the coefficient $k_{1y} = 10\ Gb$, which led to greatly overestimated results because the dislocation density was not taken into account in this coefficient.

In the present work, the evaluation of the strengthening due to laths/subgrains with low-angle boundaries was carried out using expression (10) with two different coefficients: k_{1y} = 86.2 MPa μm^{-2}

[18, 20, 23, 26], which was the original value in Eq. (10), and k_{1y} = 115–123 MPa μm^{-2} [21, 22, 24, 25], which was modified and included the dislocation strengthening.

The comparison of calculated contribution with experimental proof tensile

Table 3 summarizes all of the estimated strengthening contributions, together with the experimentally obtained yield strengths under various heat treatment conditions. The strengthening due to lattice friction, solid solution strengthening, precipitation strengthening, work hardening, and strengthening due to grains with high-angle boundaries were independent of the heat treatment conditions, whereas the dislocation strengthening and strengthening due to subgrains with low-angle boundaries significantly decreased when the tempering temperature increased. In the present work, a good agreement was found between the calculated contributions and experimental yield strength values given by the three estimation options represented in Fig. 7. The three estimation options differed from each other because of the choice of coefficient k_{1y} in the strengthening due to laths/subgrains with low-angle boundaries (10) and taking into account the dislocation strengthening (2,5) and strengthening due to grains with high-angle boundaries (9).

The contributions from different strengthening mechanisms are usually summarized in a linear manner, considering them independent of each other. On the other hand, some authors [35–37] have suggested using the root mean square (rms) summation $\sigma_{\text{rms}} = \sqrt{\sigma_{\text{A}}^2 + \sigma_{\text{B}}^2}$. In these works [35–37], σ_{A} and σ_{B} have been identified as two strengthening contributions associated with two distinct types of obstacles, where σ_{A} represents the strengthening due to the dislocations calculated by formula (2) and σ_{B} indicates all other types of strengthening. In the present work, both a linear summation and rms summation were used to estimate the overall strength.

Estimation No. 1 suggested a linear summation of the following contributions:

$$\sigma_{\text{YS}} = \sigma_i + \sigma_{\text{ss}} + \sigma_{\text{wh}} + \sigma_{\text{part}} + 122(2l)^{-1} \quad (11)$$

where l is the mean transverse width of the martensitic laths/subgrains (μm). Coefficient $\boldsymbol{k_{1y}}$ in the strengthening due to laths/subgrains with low-angle boundaries includes the dislocation strengthening [22, 24, 25]. The linear summation of estimation No. 1 gives errors of − 4.9%, − 5.2%, and − 3.3% for tempering at T = 750 °C, 770 °C, and 800 °C, respectively, when compared with the experimental yield strength values (Fig. 7).

Estimation No. 2 suggested a linear summation of the following contributions:

$$\sigma_{\text{YS}} = \sigma_i + \sigma_{\text{ss}} + \sigma_{\text{disl}} + \sigma_{\text{wh}} + \sigma_{\text{part}} + 86.2(2l)^{-1} \quad (12)$$

where l is the mean transverse width of the martensitic laths/subgrains (μm). Estimation No. 2 included both contributions from strengthening due to laths/subgrains with low-angle boundaries with the original coefficient in the Langford–Cohen model and strengthening due to the dislocations. Estimation No. 2 with linear summation gives errors of + 4.5%, + 2.8%, and + 6.6% for the tempering conditions at T = 750 °C, 770 °C, and 800 °C, respectively, when compared with the experimental values of yield stress (Fig. 7).

Table 3 Strengthening contributions, together with experimental values of yield stress after various heat treatment regimens

Strengthening contribution, MPa	750 °C tempering	770 °C tempering	800 °C tempering
σ_i	17	17	17
σ_{ss} (1)	206	209	210
σ_{disl} (2)	142	112	109
σ_{disl1} (5)	141	120	104
σ_{wh}	49	46	47
σ_{part} (6)	117	97	103
σ_{HP} (9)	206	206	206
σ_{lath} (10) for k_{1y} = 122 MPa μм$^{-2}$	247	201	168
σ_{lath} (10) for k_{1y} = 86.2 MPa μм$^{-2}$	185	151	126
Experimental YS	685 ± 30	614 ± 40	574 ± 36

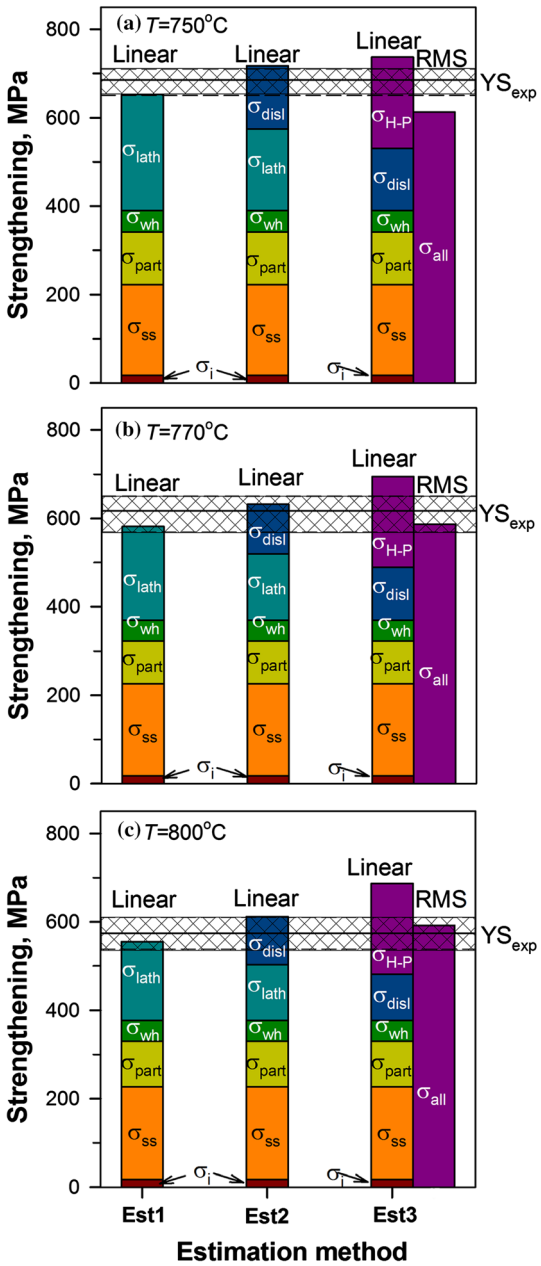

Figure 7 Different approaches to estimation of strengthening contributions for 12%Cr–3%Co martensitic steel.

Estimation No. 3 suggested both a linear summation and an rms summation of the following contributions:

$$\sigma_{\mathrm{YS}} = \sigma_i + \sigma_{\mathrm{ss}} + \sigma_{\mathrm{wh}} + \sigma_{\mathrm{part}} + \alpha GbA/(l - B) + \sigma_{H-P} \tag{13}$$

and

$$\sigma_{\mathrm{YS}} = \sqrt{\begin{array}{c}(\alpha GbA/(l - B))^2 + \\ +\left(\sigma_i + \sigma_{\mathrm{ss}} + \sigma_{\mathrm{wh}} + \sigma_{\mathrm{part}} + \sigma_{H-P}\right)^2\end{array}} \tag{14}$$

where l is the mean transverse width of the martensitic laths/subgrains (μm). Estimation No. 3 included both contributions from the strengthening due to the dislocations estimated by Eq. (5), which suggests that this strengthening includes the subgrain contribution [30], because the lath boundaries and dislocations are sources of internal elastic long-range stress fields, and the strengthening due to grains with high-angle boundaries. Estimation No. 3 with a linear summation gives errors of + 7.6%, + 13.3%, and + 19.7% for tempering at T = 750 °C, 770 °C, and 800 °C, respectively, when compared with the experimental values of yield strength (Fig. 6). Estimation No. 3 with an rms summation gives errors of − 10.6%, − 4.3%, and − 3.2% for tempering at T = 750 °C, 770 °C, and 800 °C, respectively, when compared with the experimental value of yield strength (Fig. 7). The significant overestimations of the overall strength with both the linear and rms summations indicate that the strengthening due to the grains with high-angle boundaries does not appear in the material studied, because there is a negligible feasibility that dislocations can smoothly overcome a distance equal to the block size (1.9 μm) in the TMLS, in which (Ta,Nb)X particles are homogeneously distributed inside martensitic laths and lath boundaries are decorated by $M_{23}C_6$ particles. In the works [26, 30, 51], the authors also suggest that the contribution to the yield strength from strengthening due to grains with high-angle boundaries is negligible in the model.

The experimental slope $k_{1y} \sim 138$ MPa μm^{-2} from the Langford–Cohen model (10) was calculated from the plot shown in Fig. 8a, which represents the YS versus $(2l)^{-1}$ dependence for σ_0 = 375 MPa. The experimental slope $k_{1y} \sim 75$ MPa μm^{-2} from the Langford–Cohen model (10) was calculated from the plot shown in Fig. 8b, which represents the YS − σ_{disl} versus $(2l)^{-1}$ dependence for σ_0 = 375 MPa. The value of dislocation strengthening, which depended on the tempering temperature, was removed from the experimental value of yield stress to obtain the "true" value of the slope. This "true" value of the slope was close to the original coefficient in the Langford–Cohen model [18]. Thus, the original coefficient k_{1y} = 86.2 MPa μm^{-2} from the Langford–Cohen model [18] could be used when calculating the strengthening resulting from the lath boundaries, together with the dislocation strengthening. This

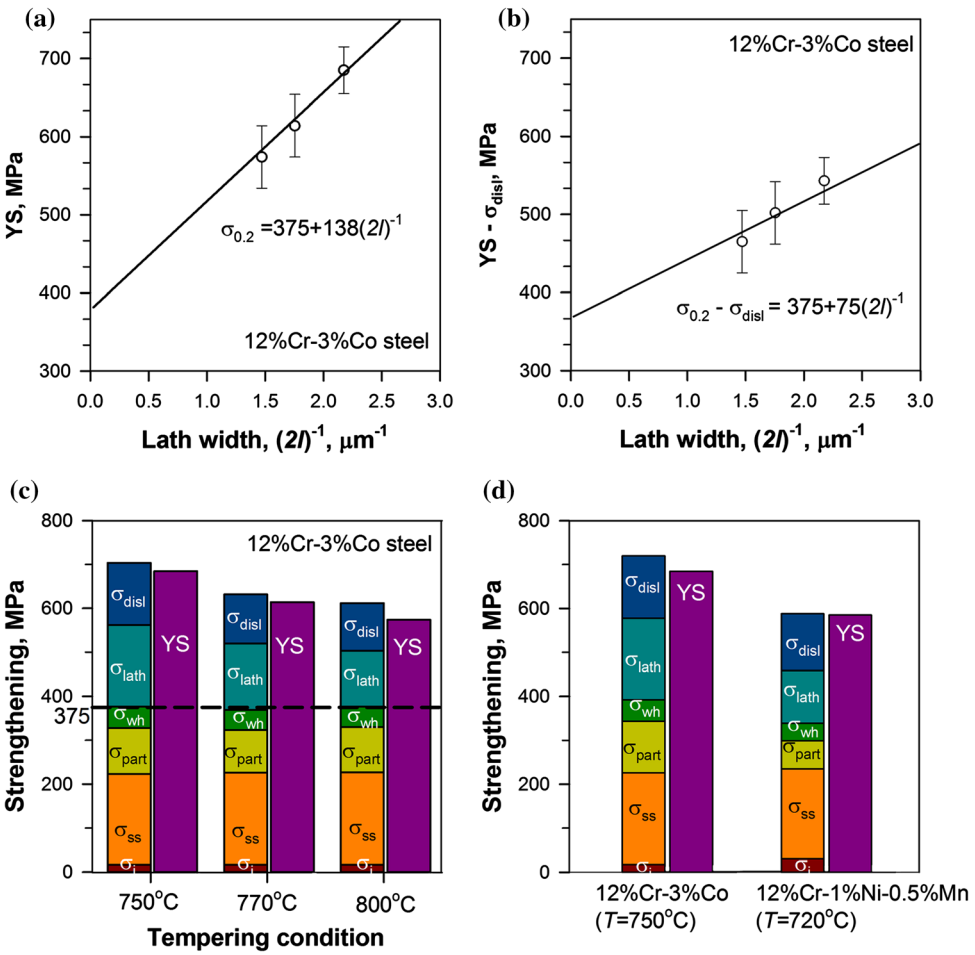

Figure 8 Experimental linear dependence between yield strength and double lath width (**a**) and linear dependence between $\sigma_{YS} - \sigma_{disl}$ and double lath width (**b**), where $\sigma_{YS} - \sigma_{disl}$ parameter is experimental yield strength, excluding dislocation strengthening; comparison between experimental and calculated yield strengths of 12%Cr–3%Co martensitic steel after various heat treatment regimens (**c**) and effect of alloying on strengthening contributions (**d**), with data for 12%Cr–1%Ni–0.5%Mn steel taken from [26].

result is in accordance with the results reported by other researchers [20, 23, 26]. Even if there is a linear dependence between the lath width and dislocation density, as seen in Eq. (5), both the strengthening due to subgrains with low-angle boundaries and dislocation strengthening have to be taken into account. The strengthening mechanism originates from the prevention of dislocation motion, and the growth of laths reduced the pinning effect on the dislocation motion [52]. Accounting for the contributions from both the subgrains and dislocations led to good agreement between the calculated strengthening contributions and experimental values for the yield strength (Figs. 7, 8). A linear summation of all the contributions using the original coefficient of $k_{1y} =$ 86.2 MPa μm^{-2} in Eq. (10) gave the best agreement between the calculated contributions and the experimental yield strength.

The strength behavior of the studied 12%Cr–3%Co steel with the low N content and high B content can be described as follows (15):

$$YS = 375 + \alpha G b \sqrt{\rho} + 75 \times (2l)^{-1} \quad (15)$$

where σ_0 = 375 MPa includes the strengthening due to the lattice friction, solid solution strengthening, precipitation strengthening, and work hardening (Fig. 8c). According to estimation No. 2, the solid solution strengthening (~ 208 MPa) and strengthening due to subgrains with low-angle boundaries made the greatest contributions to the overall strength. Moreover, the solid solution strengthening, precipitation strengthening, and work hardening were independent of the tempering temperatures, whereas subgrain strengthening and dislocation strengthening strongly depended on the tempering temperature, because the temperature determined both the lath width and dislocation density. Thus, it was obvious that a higher temperature resulted in lower contributions from both the dislocation strengthening and subgrain strengthening. When the tempering temperature increased from 750 to 800 °C, the decreases in the contributions due to subgrains

with low-angle boundaries and dislocations were 32% and 23%, respectively.

The effects of alloying on the strengthening contributions were revealed in comparison with 0.11%C–12%Cr–1Ni–0.55%Mn steel (Fig. 8d). The data for comparison were taken from [26]. The yield stress for 12%Cr–1Ni–0.55%Mn steel after tempering at 720 °C was 585 MPa [26]. The values of the solid solution strengthening and dislocation strengthening for the 12%Cr–3%Co and 12%Cr–1%Ni–0.55%Mn steel were similar despite the fact that the substitutional alloying elements were different. The solid solution strengthening values that resulted from the use of 1.5% σ(Ni,Mn) in the 12%Cr–1%Ni–0.55%Mn steel and 3% Co in the 12%Cr–3%Co steel were almost the same, and the decrease in the Si content in the 12%Cr–3%Co steel studied was compensated by an increase in the σ(W,Mo) content. Thus, cobalt provided a high level of solid solution strengthening and could replace the austenite stabilizing Ni and Mn, which have to be limited because of their strong negative effects on the creep properties [53]. A high boron content and tantalum additives increased the precipitation strengthening by decreasing the average size of the $M_{23}C_6$ carbides and the precipitation of Ta-rich MX carbonitrides after heat treatment. The increase in the particle hardening of the 12%Cr–3%Co steel was approximately 55 MPa, which demonstrated the efficiency of alloying using boron and tantalum. The work hardening was also independent of the alloying and/or heat treatment. This was in accordance with the results reported in previous paper [23, 26], in which the work hardening was independent of the heat treatment conditions and had a range of 40–65 MPa for steels with a C content of 0.1–0.4 wt%. The lath thickness in the 12%Cr–3%Co steel was less than that of the 12%Cr–1%Ni–0.55%Mn steel [26]. Thus, the strengthening due to subgrains with low-angle boundaries for the 12%Cr–1%Ni–0.55%Mn steel was half that reported in the original work [26] using coefficient k_{1y} = 86.2 MPa μm^{-2}, because double the mean transverse size of the martensitic laths/subgrains was assumed in Eq. (10), as recommended in [50]. This led to good agreement between the calculated contributions and experimental value of YS in [26], even using a linear summation. The subgrain strengthening increase in the 12%Cr–3%Co steel was approximately 65 MPa. The addition of Co and Cu instead Ni and Mn, together with the low N and high B contents in the 12%Cr–3%Co steel, provided a +100 MPa increase in the yield stress of the 12%Cr–3%Co steel (tempered at 750 °C) in comparison with the 12%Cr–1%Ni–0.55%Mn steel (tempered at 720 °C) [26].

Thus, the TMLS after tempering was strengthened by the supersaturated solid solution with elements such as W and Co, as well as the dispersion of fine secondary phase particles that stabilized the martensitic lath boundaries, the high dislocation density, and the fine lath martensite structure. Future work will focus on establishing how the strengthening contributions change during the long-term aging and creep of the 12%Cr–3%Co steel with low nitrogen and high boron contents. This study helped to determine the type of strengthening contributions, which will be estimated after creep and aging and variant of their estimation option. The original coefficient of k_{1y} = 86.2 MPa μm^{-2} in Eq. (10) will be used for the estimation of strengthening due to laths/subgrains with low-angle boundaries after creep and aging.

Conclusions

(1) A linear summation of the strengthening contributions due to the lattice friction, solid solution strengthening, work hardening, precipitations, dislocations, and subgrains when using the original coefficient k_{1y} = 86.2 MPa μm^{-2} gave the best agreement between the calculated contributions and the experimental yield strength.

(2) The correlations between the lath/subgrain size, dislocation density, and yield strength of the 12%Cr–3%Co steel with low N and high B contents after various heat treatments were revealed. The dislocation density and lath/subgrain size could be related as follows: $\rho^{0.5} = 5.41/(l + 0.07)$. The strength behavior of the studied 12%Cr–3%Co steel can be described as follows:

$$\sigma_{YS} = 375 + \sigma_{disl} + 75 \times (2l)^{-1}$$

where σ_0 = 375 MPa includes the strengthening due to the lattice friction, solid solution strengthening, precipitation strengthening, and work hardening.

(3) The solid solution strengthening (~ 208 MPa) and strengthening due to subgrains with low-angle boundaries made the greatest contributions to the overall strength. Moreover, the solid solution strengthening, precipitation strengthening, and work hardening were independent of the tempering temperature, whereas the strengthening due to subgrain boundaries and dislocations strongly depended on the tempering temperature, because this temperature determined both the lath width and dislocation density. The subgrain boundaries and dislocations made smaller contributions to the strengthening when the temperature was higher.

(4) A high boron content and tantalum additives increased the precipitation strengthening by 82% as a result of decreasing the average size of the $M_{23}C_6$ carbides and the precipitation of Ta-rich MX carbonitrides in comparison with the 12%Cr–1%Ni–0.55%Mn steel. The addition of Co and Cu instead Ni and Mn, together with low N and high B contents, decreased the transverse size of the martensitic laths, which increased the subgrain strengthening by 55% in comparison with the 12%Cr–1%Ni–0.55%Mn steel. On the other hand, the differences in the alloying elements of these steels did not affect the solid solution strengthening, dislocation strengthening, and work hardening.

Acknowledgements

The study was financially supported by Ministry for Scientific Research and Higher Education in Russian Federation, President Grant for PhD—young scientists (Grant No. 075-15-2019-1165). The authors are grateful to the staff of the Joint Research Center, «Technology and Materials» , Belgorod State University, for their assistance with instrumental analysis.

Compliance with ethical standards

Conflict of interest The authors declare that they have no conflict of interest.

References

[1] Abe F, Kern T-U, Viswanathan R (2008) Creep-resistant steels. Woodhead Publishing in Materials, Sawston

[2] Kaybyshev R, Skorobogatykh V, Shchenkova I (2010) New martensitic steels for fossil power plant: creep resistance. Phys Met Metall 109:186–200

[3] Kern T-U, Staubli M, Scarlin B (2002) The European efforts in material development for 650 °C USC power plants-COST522. ISIJ Int 42:1515–1519

[4] Kostka A, Tak K-G, Hellmig RJ, Estrin Y, Eggeler G (2007) On the contribution of carbides and micrograin boundaries on the creep strength of tempered martensite ferritic steels. Acta Mater 55:539–550

[5] Abe F (2016) Progress in creep-resistant steels for high efficiency coal-fired power plants. J Press Vessel Technol 138:040804

[6] Eggeler G, Earthman JC, Nilsvang N, Ilshner B (1989) Microstructural study of creep rupture in a 12% chromium ferritic steel. Acta Metall 37:49–60

[7] Szabo PJ (2004) Microstructural development of creep resistant ferritic steel during creep. Mater Sci Eng A 387–389:710–715

[8] Wang Y (2009) Development of new 11%Cr heat resistant ferritic steels with enhanced creep resistance for steam power plants with operating steam temperature up to 650 °C. Mater Sci Eng A 510–511:180–184

[9] Koukal J, Sondel M, Schwarz D, Foldyna V (2011) Development and microstructure of advanced creep resistant ferritic steels. J Microstruct Mater Prop 6:122–131

[10] Panait C, Bendick W, Fuchsmann A, Gourgues-Lorenzon A-F, Besson J (2010) Study of the microstructure of the Grade 91 steel after more than 100 000 h of creep exposure at 600 °C. J Press Vessel Pip 87:326–335

[11] Fedoseeva A, Dudova N, Glatzel U, Kaibyshev R (2016) Effect of W on tempering behaviour of a 3%Co modified P92 steel. J Mater Sci 51:9424–9439. https://doi.org/10.1007/s10853-016-0188-x

[12] Fedoseeva A, Dudova N, Kaibyshev R (2016) Creep strength breakdown and microstructure evolution in a 3%Co modified P92 steel. Mater Sci Eng A 654:1–12

[13] Fedoseeva A, Dudova N, Kaibyshev R (2016) Creep behavior and microstructure of a 9Cr–3Co–3W martensitic steel. J Mater Sci 52:2974–2988. https://doi.org/10.1007/s10853-016-0595-z

[14] Fedoseeva A, Dudova N, Kaibyshev R (2016) Effect of tungsten on a dispersion of M(C, N) carbonitrides in 9% Cr steels under creep conditions. Trans Indian Inst Met 69:211–215

[15] Hall EO (1951) The deformation and ageing of mild steel: III discussion of results. Proc R Soc 64:747–753
[16] Petch NJ (1953) The cleavage strength of polycrystals. J Iron Steel Inst 174:25–28
[17] Kato M (2014) Hall–Petch relationship and dislocation model for deformation of ultrafine-grained and nanocrystalline metals. Mater Trans 55:19–24
[18] Langford G, Cohen M (1969) Strain hardening of iron by severe plastic deformation. ASM-Trans 62:623–638
[19] Smith DW, Hehemann RF (1971) The influence of structural parameters on the yield strength of tempered martensite and lower bainite. J Iron Steel Inst 209:476–485
[20] Naylor JP (1979) The influence of the lath morphology on the yield stress and transition temperature of martensitic-bainitic steels. Met Trans A 10A:861–873
[21] Daigne J, Guttman M, Naylor JP (1982) The influence of lath boundaries and carbide distribution on yield strength of 0.4% C tempered martensitic steels. Mater Sci Eng 56:1–10
[22] Edmonds DV, Cochrane RC (1990) Structure-property relationships in bainitic steels. Met Trans A 21A:1527–1540
[23] Maropoulos S, Paul JDH, Ridley N (1993) Microstructure-property relationship in tempered low alloy Cr–Mo–3.5Ni–V steel. Mater Sci Technol 9:1014–1019
[24] Young CH, Bhadeshia HKDH (1994) Strength of mixtures of bainite and martensite. Mater Sci Technol 10:209–214
[25] Garcia-Mateo C, Caballero FG, Bhadeshia HKDH (2003) Development of hard bainite. ISIJ Int 43:1238–1243
[26] Li Q (2003) Modeling the microstructure-mechanical property relationship for a 12%Cr–2W–V–Mo–Ni power plant steel. Mater Sci Eng A 361:385–391
[27] Abe F (2008) Precipitate design for creep strengthening of a 9%Cr tempered martensitic steel for ultra-supercritical power plants. Sci Technol Adv Mater 9:013002 (15 pp)
[28] Shang Z, Ding J, Fan C, Song M, Li J, Li Q, Xue S, Hurtwig KT, Zhang X (2019) Tailoring the strength and ductility of T91 steel by partial tempering treatment. Acta Mater 169:209–224
[29] Maruyama K, Sawada K, Koike J (2001) Strengthening mechanisms of creep resistant tempered martensitic steel. ISIJ Int 41:641–653
[30] He SH, He BB, Zhu KY, Huang MX (2017) On the correlation among dislocation density, lath thickness and yield stress of bainite. Acta Mater 135:382–389
[31] Taylor GI (1934) The mechanism of plastic deformation of crystals. Part I.—theoretical. Proc R Soc A 145:362–388
[32] Humphreys FJ, Hatherly M (2004) Recrystallization and related annealing phenomena, 2nd edn. Elsevier, Amsterdam
[33] Lacy CE, Gensamer M (1944) The tensile properties of alloyed ferrites. Trans ASM 9:118–125
[34] Mouawad B, Boulnat X, Fabreque D, Perez M, de Carlan Y (2015) Tailoring the microstructure and the mechanical properties of ultra-fine grained high strength ferritic steels by powder metallurgy. J Nucl Mater 465:54–62
[35] Kocks UF, Argon Ali S, Ashby MF (1975) Thermodynamics and kinetics of slip. Prog Mater Sci 19:156–291
[36] Irvine J, Baker TN (1984) The influence of rolling variables on the strengthening mechanisms operating in niobium steels. Mater Sci Eng 64:123–134
[37] Kassner ME, Miller AK, Sherby OD (1982) The separate roles of subgrains and forest dislocations in the isotropic hardening of type 304 stainless steel. Met Trans A 13A:1977–1986
[38] Fedoseeva A, Tkachev E, Dudko V, Dudova N, Kaibyshev R (2017) Effect of alloying on interfacial energy of precipitation/matrix in high-chromium martensitic steels. J Mater Sci 52:4197–4209. https://doi.org/10.1007/s10853-016-0654-5
[39] Dudko VA, Fedoseeva AE, Belyakov AN, Kaibyshev RO (2015) Influence of the carbon content on the phase composition and mechanical properties of P92-type steel. Phys Met Metall 116:1165–1174
[40] Fedoseeva AE, Kozlov PA, Dudko VA, Skorobogatykh VN, Shchenkova IA, Kaibyshev RO (2015) Microstructural changes in steel 10Kh9V2MFBR during creep for 40000 hours at 600 °C. Phys Met Metall 116:1047–1056
[41] Kipelova AY, Belyakov AN, Skorobogatykh VN, Shchenkova IA, Kaibyshev RO (2010) Tempering-induced structural changes in steel 10Kh9K3V1M1FBR and their effect on the mechanical properties. Met Sci Heat Treat 52(3–4):100–110
[42] Fedorova I, Kostka A, Tkachev E, Belyakov A, Kaibyshev R (2016) Tempering behavior of a low nitrogen boron-added 9%Cr steel. Mater Sci Eng, A 662:443–455
[43] Dudova N, Kaibyshev R (2011) On the precipitation sequence in a 10%cr steel under tempering. ISIJ Int 51:826–831
[44] Nabarro FRN (1947) Dislocations in a simple cubic lattice. Proc Phys Soc 59:256–272
[45] Speich GR, Swann PRJ (1965) Yield strength and transformation substructure of quenched iron–nickel alloys. Iron Steel Inst 203:480–485
[46] Kipelova AY, Belyakov AN, Skorobogatykh VN, Shchenkova IA, Kaibyshev RO (2010) Structural changes in steel 10Kh9K3V1M1FBR due to creep. Met Sci Heat Treat 52(3–4):118–127
[47] Susila P, Sturm D, Heilmaier M, Murty BS, Subramanya Sarma V (2011) Effect of yttria particle size on the microstructure and compression creep properties of nanostructured oxide dispersion strengthened ferritic (Fe–12Cr–2W–0.5Y2O3) alloy. Mat Sci Eng A 528:4579–4584

[48] Wang Ch, Wang M, Shi J, Hui W, Dong H (2008) Effect of microstructural refinement on the toughness of low carbon martensitic steel. Scr Mater 58:492–495

[49] Barrett R, O'Donoghue P, Leen S (2018) A physically-based high temperature yield strength model for 9Cr steels. Mater Sci Eng A 730:410–424

[50] Zhang X, Godfrey A, Huang X, Hansen N, Liu Q (2011) Microstructure and strengthening mechanisms in cold-drawn pearlitic steel wire. Acta Mater 59:3422–3430

[51] Xiao B, Xu L, Tang Z, Zhao L, Jing H, Han Y, Li H (2019) A physical-based yield strength model for the microstructural degradation of G115 steel during long-term creep. Mater Sci Eng A 747:161–176

[52] Mitsuhara M, Yamasaki S, Miake M, Nakashima H, Nishida M, Kusumoto J, Kanaya A (2016) Creep strengthening by lath boundaries in 9Cr ferritic heat-resistant steel. Phil Mag Lett 96:76–83

[53] Kaibyshev R, Mishnev R, Tkachev E, Dudova N (2016) Effect of Ni and Mn on the creep behaviour of 9–10%Cr steels with low N and high B. Trans Indian Inst Met 69:203–210